High-Strength Liquid Crystal Polymer-Graphene Oxide Nanocomposites from Water

Fox, Ryan J.; Hegde, Maruti; Cole, Daniel P.; Moore, Robert B.; Picken, Stephen J.; Dingemans, Theo J.

DOI
10.1021/acsami.2c00186

Publication date
2022

Document Version
Final published version

Published in
ACS Applied Materials and Interfaces

ACS APPLIED MATERIALS & INTERFACES

www.acsami.org

Research Article

High-Strength Liquid Crystal Polymer–Graphene Oxide Nanocomposites from Water

Ryan J. Fox, Maruti Hegde, Daniel P. Cole, Robert B. Moore, Stephen J. Picken, and Theo J. Dingemans*

Cite This: *ACS Appl. Mater. Interfaces* 2022, 14, 16592–16600

Read Online

ACCESS | Metrics & More | Article Recommendations | Supporting Information

ABSTRACT: We report on the morphology and mechanical properties of nanocomposite films derived from aqueous, hybrid liquid crystalline mixtures of rodlike aggregates of a sulfonated, all-aromatic polyamide, poly(2,2′-disulfonyl-4,4′-benzidine terephthalamide) (PBDT), and graphene oxide (GO) platelets. An isothermal step at 200 °C facilitates in situ partial thermal reduction of GO to reduced GO (rGO) in nanocomposite films. X-ray scattering studies reveal that PBDT–rGO nanocomposites exhibit both higher in-plane alignment of PBDT (the order parameter increases from 0.79 to 0.9 at 1.8 vol % rGO) and alignment along the casting direction (from 0.1 to 0.6 at 1.8 vol % rGO). From dynamic mechanical thermal analysis, the interaction between PBDT and rGO causes the β-relaxation activation energy for PBDT to increase with rGO concentration. Modulus mapping of nanocomposites using atomic force microscopy demonstrates enhanced local stiffness, indicating reinforcement. From stress–strain analysis, the average Young's modulus increases from 16 to 37 GPa at 1.8 vol % rGO and the average tensile strength increases from 210 to 640 MPa. Despite polymer alignment along the casting direction, an average transverse tensile strength of 230 MPa is obtained.

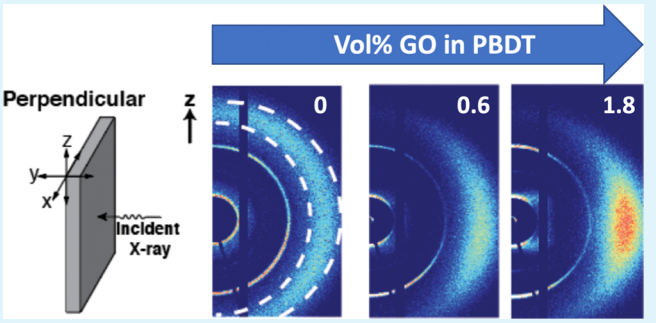

KEYWORDS: *nanocomposite, hybrid liquid crystal, graphene oxide, reduced graphene oxide, mechanical reinforcement*

1. INTRODUCTION

In a polymeric nanocomposite material, the role of the nanoinclusion is to enhance one or more physical properties, with the usual target properties being electrical or mechanical.[1−5] While most previous studies have focused mostly on nanocomposites formed from simple linear polymers and nanoparticles, this work demonstrates the effectiveness of bringing together two different types of highly anisotropic molecular structures to form a stiff and robust nanocomposite. The maximum attainable mechanical enhancement in a polymer nanocomposite depends on stress transfer from the polymer matrix to the nanofiller, which in turn is predicated on several interdependent factors such as interfacial adhesion, dispersion quality, filler aspect ratio, and its alignment in the polymer matrix.[6−9] The challenges in preparing reinforced polymer nanocomposites using 2D platelets such as graphene oxide (GO) lie in obtaining well-dispersed and extended GO platelets that are aligned in-plane within the composite. Toward this end, the self-organization capability of GO in the lyotropic, liquid crystalline (LC) phase[10−14] in combination with polymer processing methods can be exploited to produce reinforced nanocomposites.[9,15−18] Our recent discovery harnessed molecular self-organization of GO and a rodlike polymer in the LC phase to obtain highly reinforced polymeric nanocomposites.[19] Simple mixing of a uniaxial, colloidal, discotic nematic (N^- phase) GO and a uniaxial, calamitic nematic solution of a sulfonated, rodlike, all-aromatic aramid poly(2,2′-disulfonyl-4,4′-benzidine terephthalamide) (PBDT) (N^+ phase)[20−30] resulted in a stable supramolecular organization characterized as a hybrid LC (nematic) phase (^hN). In particular, we studied the hybrid biaxial nematic (^hN_b)[31] mixture wherein the mesoscopic GO director $\mathbf{n}_{GO}$ and PBDT director $\mathbf{n}_p$ are orientationally correlated and locally orthogonal to each other.[19] The dispersed GO was stable in the ^hN_b phase, making this the first instance of a stable rod-plate hybrid biaxial mixture. PBDT–GO nanocomposite films prepared from film casting of these hybrid precursor mixtures exhibit a stratified, uniplanar morphology with extremely good mechanical properties: a Young's modulus of ∼38 GPa and a tensile strength of ∼620 MPa.

Received: January 4, 2022
Accepted: March 16, 2022
Published: March 25, 2022

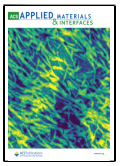

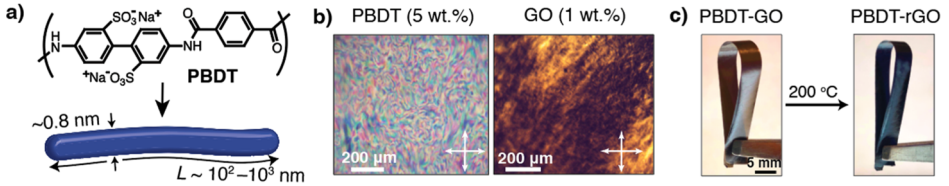

Figure 1. Mesogenic components and their nanocomposites: (a) molecular structure of PBDT. In aqueous solutions, PBDT forms a dimer having a double helical conformation that in turn forms rodlike aggregates with high persistence length. (b) The high aspect ratio of PBDT rods and GO platelets makes them mesogenic, resulting in birefringent, nematic textures when PBDT solutions and GO colloids above the critical concentration are viewed between crossed polarizers of an optical microscope. (c) Digital photographs of a nanocomposite film prepared by mixing nematic solutions of PBDT and GO before (left) and after (right) in situ thermal reduction of GO to rGO at 200 °C under N_2. Thermal reduction of GO to rGO causes the nanocomposite color to change from brown to black.

Our previous work[19] was performed using a fixed mass ratio of PBDT and GO (2.44 wt % GO). This raises pertinent questions: how do nanocomposite properties such as morphology and mechanical properties vary with GO concentration? For this work, we have limited ourselves to understanding the solid-state properties of nematic nanocomposite films rather than identifying the phases formed by hybrid nematic (^{h}N) precursor mixtures. We will demonstrate that simple mixing of GO and PBDT results in stable, LC precursor hybrid (^{h}N) mixtures that on drying and partial GO reduction yield mechanically reinforced nanocomposite films. Additionally, using X-ray scattering, we attempt to understand the origin of reinforcement in these nanocomposites. We also demonstrate how secondary relaxations of PBDT are perturbed by the interactions between PBDT and GO. Most importantly, this work demonstrates that rigid-rod polyelectrolytes are ideal matrix polymers for GO-based reinforced nanocomposites.

2. RESULTS AND DISCUSSION

2.1. LC Components, Precursor Hybrid Mixtures, and Nanocomposite Films. An interfacial polymerization route[27] afforded PBDT (Figure 1a) having a viscosity average molecular weight (M_v) of ~19 kg/mol (see Figure S1, Table S1, and associated discussion in the Supporting Information). The Hummers method enabled preparation of graphite oxide from natural graphite.[32] Subsequent purification and fractionation yield aqueous, colloidal GO with an average platelet diameter of 1.3 ± 0.3 μm [scanning electron microscopy (SEM) images are provided in Figure S2, Supporting Information] and a degree of functionalization, that is, C/O ratio, of 2.6 from XPS measurements. The birefringent uniaxial nematic phases of PBDT (N^+ phase) and GO (N^- phase) in water are shown in Figure 1b.

Simple mixing of nematic PBDT aqueous solutions (Figure 1b) and colloidal GO with continuous stirring yields hybrid LC precursor mixtures wherein the GO dispersion is stable.[19] These were prepared such that the concentration of PBDT (C_{PBDT}) in all resultant final hybrid precursor mixtures is 5 wt % (see the experimental section and Table 1), whereas the concentration of GO (C_{GO}) is varied depending on the target GO loading (0.016–0.151 wt %).

Film casting was performed by deposition of these LC PBDT–GO precursor mixtures onto glass substrates and film casting with a doctor blade at a shear rate of 5 s^{-1}. Drying at 60 °C (~2 h) in air yields nematic nanocomposite films containing homogeneously dispersed GO. The obtained films are hydrophilic and absorb up to ~20 wt % water under ambient humidity conditions, thereby lowering its mechanical performance and obscuring PBDT's secondary β-relaxation that occurs below 100 °C.[33] Since we are primarily interested in knowing the maximum attainable reinforcement, water removal was achieved by drying the films at 200 °C prior to testing (Figure S3, Supporting Information). However, at 200 °C, GO undergoes in situ thermal reduction to partially reduced GO (rGO)[34] as evidenced by a 30% mass reduction (Figure S4A,B, Supporting Information) and a concomitant increase in C/O ratio from 2.6 to 6.5 (Figure S4C, Supporting Information). We accounted for the GO weight loss during thermal reduction when reporting the rGO concentration in the nanocomposite film; for example, drying of a hybrid precursor mixture with C_{GO} = 0.151 wt % yields a nanocomposite film with 3.0 wt % GO, which on thermal reduction to rGO translates to 2.1 wt % rGO (1.8 vol % rGO) (Table 1). Although the thermal reduction of GO to rGO results in a color change from light brown to black, the free-standing films remain flexible and mechanically robust (Figure 1c). No change in decomposition temperature was observed for the nanocomposites as compared to the neat polymer (Figure S5, Supporting Information).

Table 1. PBDT and GO Concentrations in the Precursor Hybrid LC Mixture and the Corresponding GO Loading in Solid-State Nanocomposite Films before and after In Situ Thermal Reduction of GO

	in precursor hybrid mixtures			in solid nanocomposite films		
	C_{total}[a] (wt %)	C_{PBDT} (wt %)	C_{GO} (wt %)	GO[b] wt %	rGO[c] wt %	rGO vol %
1	5.02	5.0	0.016	0.3	0.2	0.2
2	5.03	5.0	0.033	0.7	0.5	0.4
3	5.05	5.0	0.050	1.0	0.7	0.6
4	5.10	5.0	0.100	2.0	1.4	1.2
5	5.13	5.0	0.125	2.5	1.8	1.5
6	5.15	5.0	0.151	3.0	2.1	1.8

[a] C_{total} = total solids concentration in hybrid precursor mixtures. [b] The mass fraction of GO in solid-state nanocomposite films is obtained using $C_{GO}/(C_{GO} + C_{PBDT})$. [c] The reported rGO wt % accounts for 30% weight loss due to partial thermal reduction of GO at 200 °C.

2.2. Morphology of PBDT–rGO Nanocomposite Films. Wide-angle X-ray scattering (WAXS) in two configurations enables study of the structure of PBDT–GO nanocomposites films. In the perpendicular X-ray configuration, the incident X-ray beam is parallel to the film surface normal (along the *y*-axis), thus providing information on PBDT alignment along the casting direction (*z*-axis, *x*–*z* plane) (Figure 2a). In the parallel X-ray configuration (Figure 2b), the incident X-ray beam is orthogonal to surface normal, enabling analysis of in-plane polymer alignment, that is, in the *y*–*z* plane.[19,22,35]

https://doi.org/10.1021/acsami.2c00186
ACS Appl. Mater. Interfaces 2022, 14, 16592–16600

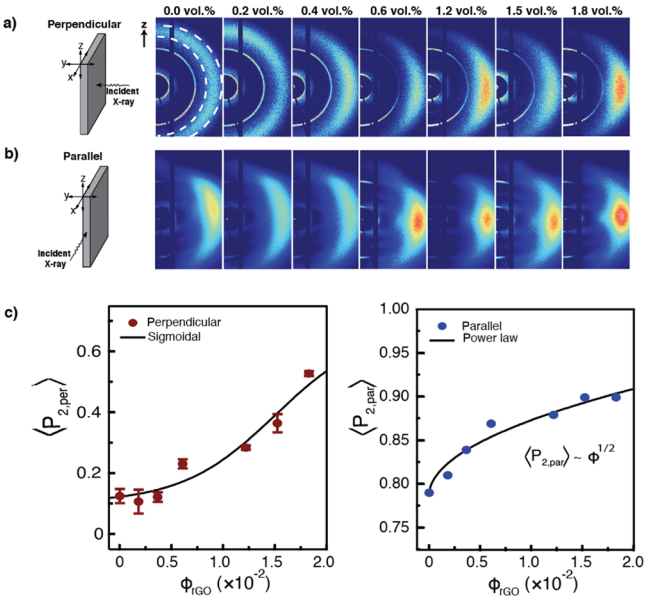

Figure 2. WAXS of PBDT−rGO nanocomposite films: (a) 2D WAXS patterns of neat PBDT and nanocomposite films in the perpendicular configuration. The film casting direction is along the *z*-axis, and the film surface normal is parallel to the *y*-axis. (b) 2D WAXS patterns in the parallel configuration provide information on uniplanar polymer alignment, that is, in the *y*−*z* plane. For both configurations, the azimuthal intensity dependence of the interchain scattering peak (marked by two dotted lines in Figure 2a) increases with rGO concentration due to increasing PBDT orientation along the *z*-axis. (c) The polymer ordering in either plane (configuration) can be calculated using the scattering that corresponds to the interchain distance (3.8 Å). The order parameter along the casting direction, as measured in the perpendicular configuration, increases sigmoidally, whereas the parallel order parameter exhibits a power law increase as a function of rGO concentration.

The nanocomposite films exhibit an increase in azimuthal dependence of scattering intensity from intermolecular and intramolecular periodicities in PBDT (Figure 2a,b). The average degree of PBDT alignment can be computed using the scattering intensity associated with interchain spacing (q = 1.7 Å^{-1}, d = 3.8 Å) (highlighted by two dotted white lines in Figure 2a).[19,22] Using a Maier−Saupe distribution function, the scattering intensity can be used to obtain a distribution function (equations are provided in the Supporting Information below Figure S6) which can be utilized to compute the average order parameter in the two planes, $\langle P_{2,\mathrm{per}}\rangle$ and $\langle P_{2,\mathrm{par}}\rangle$ (Figures 2c and S6).[19,33,36,37]

The mechanistic origins for PBDT alignment in the two planes are different; hence, there are two different trends in $\langle P_2\rangle$ as a function of rGO concentration. The neat PBDT film exhibits a polydomain nematic structure as polymer relaxation during the relatively slow drying process yields a nearly isotropic distribution of nematic domain directors (for the neat PBDT film, $\langle P_{2,\mathrm{per}}\rangle$ = 0.1); that is, $\mathbf{n}_p$ has a low degree of long-range order at length scales greater than the nematic domain structure. However, when hybrid precursor mixtures are cast as films, tangential anchoring of PBDT on the GO surface and higher dispersion viscosity[38] inhibit the orientational relaxation of PBDT domains. This is manifested in a sigmoidal increase in $\langle P_{2,\mathrm{per}}\rangle$ to 0.6 with increasing GO concentration. Despite in situ thermal reduction of GO to rGO at 200 °C, the polymer alignment is maintained due to a lack of long-range segmental motions—PBDT does not exhibit a T_g before degradation. During drying, affine deformation[21,31] causes PBDT to preferentially adopt a uniplanar orientation with respect to the glass casting substrate ($\langle P_{2,\mathrm{par}}\rangle \sim 0.79$); that is, $\mathbf{n}_p$ is parallel to the casting substrate. Our previous study on hybrid biaxial precursor mixtures revealed that shearing causes uniplanar alignment of both GO and PBDT.[19] The propensity for uniplanar alignment is enhanced on drying the precursor mixtures to obtain solid films. The extent of parallelism of $\mathbf{n}_p$ (in the *y*−*z* plane) increases with rGO content in the nanocomposite films; $\langle P_{2,\mathrm{par}}\rangle$ increases to 0.9 at 1.8 vol % rGO from 0.79. In the affine deformation model, the yield stress that acts on GO and PBDT in the hybrid precursor mixtures is expected to be inversely proportional to the critical total solids concentration, that is, the concentration at which gelation occurs.[37] With increasing concentration of GO in the hybrid precursor mixtures and hence a larger density of PBDT−GO networks, the development of a yield stress during drying can occur at a lower critical solids concentration. Such affine deformation models have been successfully applied to explain ordering in LC polymers[39,40] and clay platelet orientation in alginate-clay nanocomposites.[37] A similar mechanism can help explain the power law trend observed for $\langle P_{2,\mathrm{par}}\rangle$ in PBDT−rGO films.

In PBDT films, PBDT exists as large aggregates that can be visualized using microscopy techniques. Atomic force microscopy (AFM) images of the PBDT film surface reveal rodlike aggregates with cross-sectional dimensions ranging between 50 and 200 nm (Figure S7). Additionally, SEM of PBDT and PBDT−1.8 vol % rGO film cross-sections demonstrates that the network of these aggregates forms a layered morphology (Figure 3a). These aggregates are responsible for the low-q scattering in small-angle X-ray scattering (SAXS) patterns of films (Figure 3b). In comparison to neat PBDT, the SAXS patterns of PBDT−1.8 vol % rGO films exhibit greater

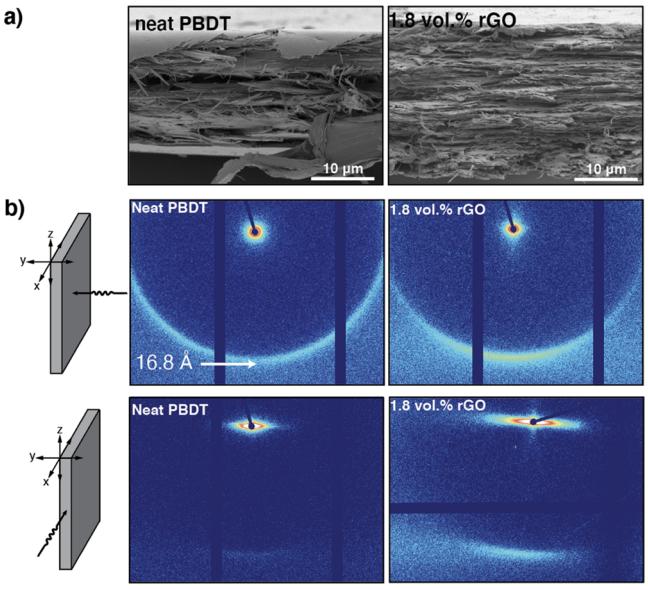

Figure 3. Morphology and structure of PBDT−rGO nanocomposites: (a) SEM images of cross-sections of neat PBDT and 1.8 vol % rGO films. Both films appear fibrillar, exhibiting a layered/stratified structure. (b) 2D SAXS patterns of neat PBDT and 1.8 vol % rGO nanocomposite in the perpendicular and parallel scattering configurations.

https://doi.org/10.1021/acsami.2c00186
ACS Appl. Mater. Interfaces 2022, 14, 16592−16600

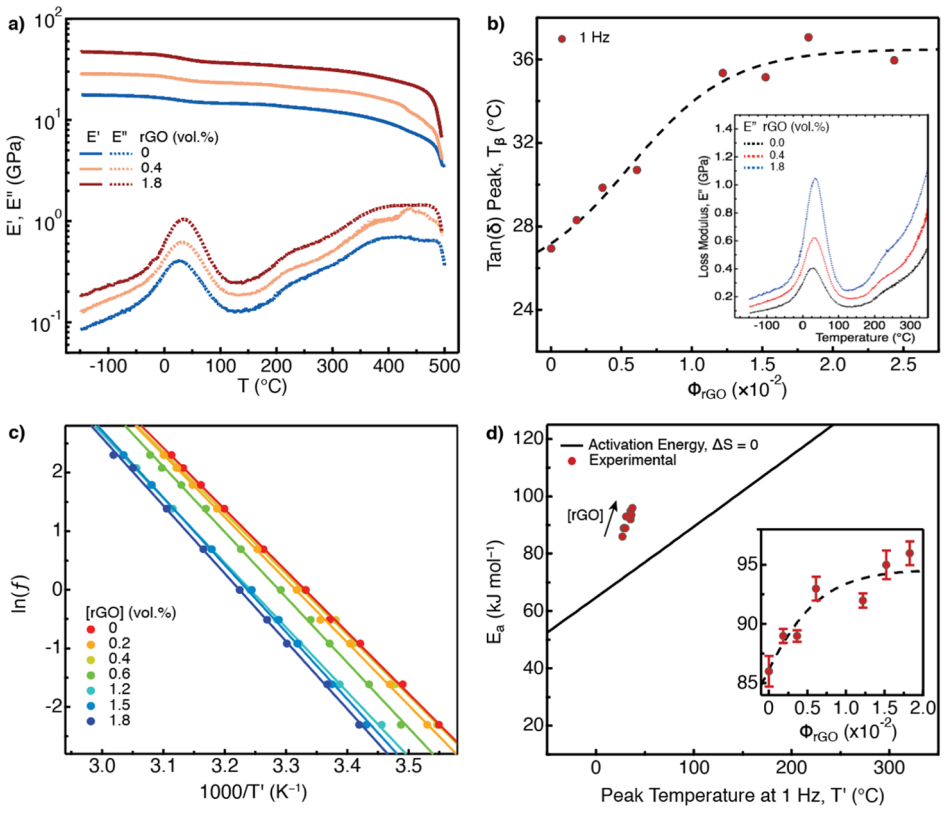

Figure 4. DMTA of PBDT−rGO nanocomposites: (a) storage (E') and loss (E'') moduli as a function of temperature at 1 Hz measured using a heating rate of 2 °C min^{-1}. (b) β-Relaxation temperature as measured by the temperature of the tan(δ) peak at 1 Hz. The dashed line is a guide to the eye. Inset: E'' as a function of temperature over the β-relaxation temperature range. (c) Arrhenius plots of the natural logarithm of mechanical oscillation frequency as a function of inverse absolute temperature of the loss tangent maximum over the β-relaxation temperature range. Linear fits indicate agreement with the Arrhenius function for this thermal relaxation. The peak loss tangent temperature is shifted to higher temperatures with increasing rGO concentration. (d) Experimental activation energies of the PBDT−rGO nanocomposites compared to the zero-entropy activation energy (solid line). The deviation from the line indicates that a complex and cooperative motional process is responsible for the relaxation.

azimuthal intensity dependence in both X-ray configurations (Figure 3b) due to increased uniplanar organization of PBDT aggregates.

2.3. Thermo-Mechanical Analysis. We used dynamic mechanical thermal analysis (DMTA) to investigate the thermo-mechanical properties of PBDT−rGO nanocomposites. Isochronal temperature ramps of the neat polymer and nanocomposite films (2 °C min^{-1}, 1 Hz) are shown in Figure 4a.

The substantial mechanical reinforcement of the nanocomposites over the neat polymer is evidenced by the significant increase in storage modulus (E') of the nanocomposites over the neat polymer. Since glassy polymers exhibit E' values that are similar to their Young's modulus, we will discuss mechanical reinforcement in the subsequent section.

Nanoparticle inclusion can perturb polymer relaxations, and these changes are reflective of polymer packing and noncovalent interactions. Although PBDT does not exhibit a glass transition (T_g) before thermal decomposition, we have previously reported two secondary relaxations using DMTA:[33] a clear peak in loss modulus (E'') and tan(δ) curves centered at ∼30 °C (Figure 4a) and a second relaxation with an onset at ∼180 °C. We have previously assigned these two transitions to β- and β*-relaxations, respectively, based on the fact that an analogous polymer, poly-*p*-phenylene terephthalamide (PPTA), exhibits secondary transitions in a similar temperature range.[41] In aromatic and semi-aromatic polyamides, this peak has been associated with complex and cooperative motions related to amide groups in the amorphous domains.[42−44] Moreover, in a large number of these polyamides, the presence of water has been shown to perturb hydrogen bonding of amide groups, resulting in an amplification of the relaxation peak. In our case, although the films are free of water, the results are analogous; the remnant oxy-functionalities on the rGO surface can still interact with amide groups in PBDT, therefore resulting in an increased relaxation peak intensity (inset, Figure 4b). The increased polymer alignment due to the presence of rGO may also act to increase the thermal energy required for the polymer to undergo these secondary relaxations. The peak temperature of the β-relaxation process from tan(δ) also increases (Figure 4b) with increasing rGO amount.

To gain a more detailed insight into the observed β-relaxation near room temperature in PBDT and the resulting nanocomposites, we investigated the nanocomposites over 2 decades of frequency (0.1 to 10 Hz) through the temperature range of −30 to 110 °C in 5 °C intervals. The loss tangent at each discrete frequency as a function of temperature for all nanocomposites is shown in Figure S8. At higher mechanical oscillation frequencies, the peak in the loss tangent is shifted to higher temperatures, consistent with the Arrhenius relationship. The activation energy E_a of the relaxation can be extracted by plotting the natural logarithm of each frequency as

https://doi.org/10.1021/acsami.2c00186
ACS Appl. Mater. Interfaces 2022, 14, 16592−16600

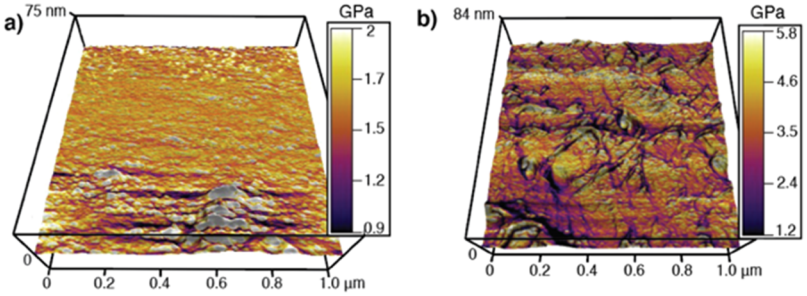

Figure 5. AFM modulus–height maps of (a) neat PBDT and (b) 1.8 vol % rGO nanocomposite. The color scale indicates the elastic modulus map values from AFM measurements.

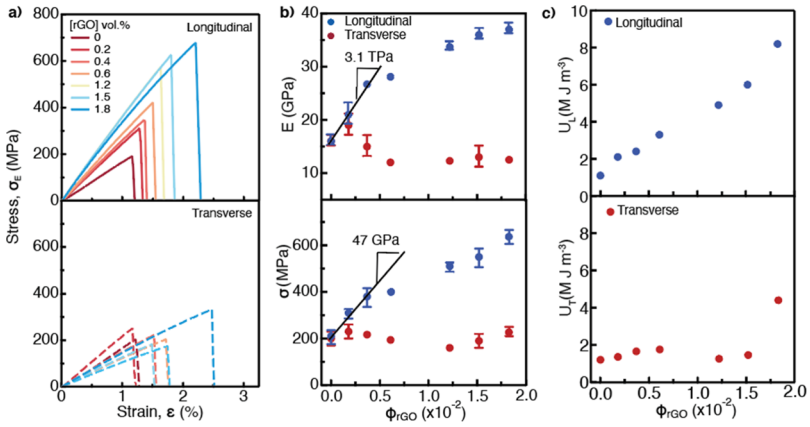

Figure 6. Mechanical properties of nanocomposite films: (a) stress–strain behavior of PBDT–rGO nanocomposites from uniaxial tension measurements at 25 °C under a N_2 atmosphere in the longitudinal (top, solid lines) and transverse (bottom, dashed lines) directions. Samples with the highest strain at break values are presented. (b) Young's modulus (top) and tensile strength (bottom) in the longitudinal (blue) and transverse (red) directions as a function of rGO concentration. The straight lines are linear fits to the low concentration region of the data. The error bars indicate the standard error of six measurements for the Young's modulus and the standard error of the best three measurements for tensile strength. (c) Toughness in the longitudinal (top) and transverse (bottom) directions as a function of rGO concentration.

Table 2. Mechanical Properties from Stress–Strain Analysis of PBDT and PBDT–rGO Nanocomposites

[rGO] (vol %)	E_L (GPa)[a]	E_T (GPa)[a]	σ_L (MPa)[b]	σ_T (MPa)[b]	$\varepsilon_{max,L}$ (%)[c]	$\varepsilon_{max,T}$ (%)[c]	U_L (MJ m^{-3})[d]	U_T (MJ m^{-3})[d]
0.0	16 ± 1	16 ± 1	210 ± 3	200 ± 30	1.3	1.2	1.1	1.2
0.2	21 ± 2	19 ± 2	310 ± 20	230 ± 30	1.6	1.2	2.1	1.5
0.4	26.7 ± 0.4	15 ± 2	380 ± 40	217 ± 6	1.6	1.5	2.4	1.8
0.6	28.1 ± 0.5	12.0 ± 0.4	400 ± 10	194 ± 6	1.5	1.7	3.3	1.9
1.2	33.7 ± 0.8	12.3 ± 0.4	510 ± 20	160 ± 10	1.6	1.5	4.9	1.4
1.5	36 ± 1	13 ± 2	550 ± 40	190 ± 30	1.8	1.7	6.0	1.6
1.8	37 ± 1	12.5 ± 0.6	640 ± 30	230 ± 20	2.2	2.5	8.2	4.4

[a]The average and standard errors of six specimens are reported. [b]The average and standard errors of three best samples are reported. [c]Best strain and toughness values achieved are reported. [d]Obtained by integration of longitudinal and transverse stress–strain curves.

a function of the inverse absolute peak temperature of the loss tangent maxima (Figure 4c). These data fall on straight lines, indicating excellent agreement with an Arrhenius process. A comparison of the experimental E_a for all rGO volume fractions with the zero-entropy E_a, calculated by eq S6, is shown in Figure 4d and as a function of rGO concentration in the inset. The E_a for the β-relaxation in neat PBDT is much higher than predicted by the zero-entropy E_a equation, suggesting a complex relaxation process. The increase in E_a with rGO concentration (from ~86 kJ mol^{-1} in the neat polymer to ~96 kJ mol^{-1} at 1.8 vol % rGO) indicates a larger energy barrier to the secondary thermal relaxation in the nanocomposites.

2.4. Mechanical Reinforcement in Nanocomposite Films. AFM modulus mapping was employed to provide insight into changes in the polymer's stiffness at the submicron scale. Both PBDT and PBDT–1.8 vol % rGO films were cryotomed, and a modulus map was constructed by measuring the cross-sectional area (Figure 5).

From the modulus maps, it is clear that larger modulus values are achieved in PBDT–rGO films, up to 5.8 GPa. Both neat PBDT and 1.8 vol % rGO nanocomposites exhibit heterogeneity in spatial distribution of stiffness. A quantitative analysis of the modulus mapping is likely to be complicated by the cryotoming process (−55 °C) and the thermomechanical–cryotome response that may perturb the local morphology.

Stress–strain measurements were performed to investigate bulk mechanical properties of the nanocomposite films. In aligned polymeric fibers and uniaxial polymer–fiber composites, the alignment of reinforcing fibers results in unidirec-

https://doi.org/10.1021/acsami.2c00186
ACS Appl. Mater. Interfaces 2022, 14, 16592–16600

tional mechanical reinforcement.[34] The use of 2D rGO flakes should result in mechanical reinforcement when stress is applied along the rGO basal plane, that is, in both the longitudinal and transverse directions of the nanocomposite film. The stress−strain curves of PBDT−rGO nanocomposites in both the longitudinal and transverse orientations to the casting direction are presented in Figure 6 top and bottom, respectively.

Neat PBDT films exhibit low strains at break (∼1.1−1.2%) without a distinct yield stress, suggesting little to no plastic deformation (Figure 6a, top), consistent with the rigid structure of the polymer backbone. The rigid backbone and polymer alignment in the neat PBDT film results in an average Young's modulus of ∼16 GPa and a tensile strength of ∼210 MPa (Table 2). The strong (non-covalent) interactions between rGO and PBDT along with the increased polymer alignment in both planes result in substantial stress−strain improvements in the longitudinal direction (Figure 6a,b and Table 2)—the 1.8 vol % rGO film exhibits a 37 GPa Young's modulus, a 640 MPa ultimate tensile strength, and a 2.2% strain at break. A maximum reinforcement efficiency is obtained in the low-concentration regime (below 0.4 vol % rGO), where $dE/d\phi = 3100 \pm 100$ GPa and $d\sigma/d\phi = 47 \pm 7$ GPa (Figure 6b).

An indirect evidence of stress transfer from PBDT to rGO is obtained by analyzing the stress−strain data in the transverse direction, that is, by measuring film properties from samples cut orthogonally to the casting direction. For such samples, the modulus can be expected to decrease with increasing polymer alignment along the casting direction. In the neat polymer, the nearly isotropic distribution of $\mathbf{n}_p$ along the casting direction results in isotropic modulus and strength values; that is, the values are the same when measured in the transverse or longitudinal directions (Figure 6a,b). However, the transverse Young's modulus as a function of rGO concentration decreases from an initial value of 16 GPa but plateaus at ∼12.5 GPa. The enhanced ductility at rGO concentrations greater than 1.8 vol % enabled an average transverse ultimate tensile strength of 230 MPa to be achieved. We postulate that these impressive mechanical properties in the transverse direction are made possible through the use of platelets as a reinforcing phase, which provides isotropic reinforcement along the basal plane of the rGO platelet. Concomitant with the increases in modulus and tensile strength, the toughness, measured as the area under the stress−strain curve, increases by nearly an order of magnitude from 1.1 to 8.2 MJ m^{-3} at 1.8 vol % rGO in the longitudinal direction (Figure 6c, top and Table 2). In the transverse direction, the increases in tensile strength and strain enable modest gains in toughness (Figure 6c, bottom andTable 2).

3. CONCLUSIONS

We have demonstrated mechanical reinforcement in PBDT−rGO nanocomposite films achieved by film-casting aqueous hybrid nematic mixtures of PBDT rods and GO platelets. Thermal treatment of a series of nanocomposite films at 200 °C causes in situ partial reduction of GO to rGO. SAXS studies reveal that the presence of rGO in PBDT inhibits polymer relaxation, resulting in increased polymer alignment (up to a 0.6 order parameter at 1.8 vol % rGO) along the film casting direction. Additionally, the presence of rGO increases the tendency of PBDT chains to adopt a uniplanar alignment; the order parameter increases from 0.79 to 0.9 at 1.8 vol % rGO. The non-covalent interactions between PBDT and rGO and enhanced ordering of PBDT result in an increase in activation energy for secondary relaxations (β-relaxation); that is, the presence of rGO increases the energy barrier for local motions of the polymer to occur. Driven by polymer alignment and a strong interface facilitated by non-covalent interactions, the nanocomposite films exhibit dramatic increases in the longitudinal Young's modulus (16 GPa to 37 GPa), ultimate strength (210 to 640 MPa), strain at break (1.2 to 2.2%), and toughness (1.1 to 8.2 MJ m^{-3}). Despite increased polymer alignment along the casting direction (longitudinal direction), stress transfer from the polymer to 2D rGO platelets results in significant improvement of the average transverse tensile strength (210 to 230 MPa) and strain at break (1.2 to 2.5%). Although this work focuses on the solid-state properties of nanocomposites, excluded volume interactions in aqueous mixtures of rods and plates can yield different LC phases depending on the concentration of the respective components. The hybrid LC mixtures prepared here with a low GO content may be uniaxial hybrid nematics ($^hN^+$), whereas hybrid mixtures with a high GO content can result in biaxial nematics (^hN_b). The challenge for future work lies in identifying and understanding which precursor mixture, that is, the $^hN^+$ phase or ^hN_b phase (biaxial phase), is ideal for preparing mechanically reinforced nanocomposite films and fibers. Understanding the phase diagram topology of the precursor mixture and the specific mechanisms for nanocomposite reinforcement will enable rapid optimization of material performance, for example, the formation of high-modulus, high-impact, and high-toughness nanocomposites.

4. EXPERIMENTAL METHODS

4.1. Materials. Terephthaloyl chloride (TPC) was purchased from Sigma-Aldrich and freshly sublimed under vacuum prior to use. 4,4′-Diaminobiphenyl-2,2′-disulfonic acid hydrate (BDSA) (95%) was purchased from Alfa Aesar. Purification of BDSA was accomplished by dissolution in NaOH and precipitation into cold EtOH, followed by filtration of the BDSA sodium salt. The salt was dissolved in water and precipitated by the addition of a stoichiometric amount of concentrated HCl (37 wt %), and the solids were collected by filtration. The process was repeated until the filtrate was clear and white crystals of BDSA were obtained. Polyethylene glycol 300 (PEG300) and sodium carbonate (Na_2CO_3) were purchased from Sigma Aldrich and used as received. Natural flake graphite (batch #: 13802EH) was purchased from Sigma-Aldrich and used as received. SpectraPor 1 dialysis membranes were purchased from Sigma Aldrich and purified of ethylene glycol with water/EtOH prior to use.

4.2. Synthesis and Molecular Weight of PBDT. An interfacial polymerization method was used as previously described by Sarkar and Kershner.[27] A 3 L round-bottom flask was used as the reaction vessel equipped with an overhead stirrer and placed in an ice bath. In a typical reaction, Na_2CO_3 (9.539 g, 90 mmol) was added with 900 mL of deionized water and dissolved with stirring. BDSA (7.748 g, 22.5 mmol) was added to the solution and mixed until dissolved. PEG300 (7.2 g, 24 mmol) was added with 300 mL of $CHCl_3$ and stirred at 2000 rpm until a white emulsion was obtained. Freshly sublimed TPC (4.568 g, 22.5 mmol) was dissolved into 300 mL of $CHCl_3$ and added to the reaction mixture while stirring at 2000 rpm. The reaction was allowed to proceed for 1 h with stirring at 2000 rpm, at which point the mixture became a gel. Rotary evaporation was used to distill the $CHCl_3$ from the emulsion to obtain the polymer in aqueous solution. The polymer was washed by repeated precipitations into acetone and dried under vacuum before use. We quantified the molecular weight using intrinsic viscosity measurements in 96% H_2SO_4 (Figure S1 and Table S1). Dilute solution viscometry measurements were carried out using a suspended level Cannon

https://doi.org/10.1021/acsami.2c00186
ACS Appl. Mater. Interfaces 2022, 14, 16592−16600

Ubbelohde capillary viscometer (model 2E-316). Dry PBDT was added to a 25 mL volumetric flask, and concentrated (96%) sulfuric acid was used to fill to the volume. The solution was shaken overnight until dissolved. 8 mL of the solution was added to the viscometer and equilibrated at 25 °C in a water bath. Measurements were taken by recording the flow time between the viscometer marks, and temperature equilibrium was checked by consecutive measurements being less than 0.5% error. Dilutions were accomplished in situ by adding pure concentrated sulfuric acid and mixing by bubbling with dry nitrogen. Using Mark−Houwink equation parameters reported for PPTA,[45] the viscosity average molecular weight of PBDT was 19 kg mol^{-1}, consistent with prior results for PBDT.[22,27] Further details on dilute solution viscosity measurements are provided in the Supporting Information.

4.3. Synthesis and Characterization of GO. Graphite oxide was prepared from natural flake graphite using the Hummers method.[32] The obtained graphite oxide slurry was washed 5× with 1 M HCl, dried in air, and then dispersed in 500 mL of deionized water. Mild bath sonication for 1 h was used to exfoliate the graphite oxide into single-layer GO, at which point the nematic texture of liquid crystal GO becomes apparent. The exfoliated dispersion was dialyzed against 10 L of deionized water for 1 week, exchanging daily. After dialysis, the exfoliated dispersion was briefly centrifuged (10^4 rpm, 2 min) to eliminate the graphitic sediment, and the supernatant (containing a broad distribution of flake sizes) was decanted. The decanted dispersion was concentrated by centrifugation at 10^4 rpm for 10 h, and the supernatant was decanted. The bottom nematic layer containing a high concentration of GO was collected for use in nanocomposite fabrication.

4.4. Preparation of Hybrid Nematic PBDT−GO Precursor Mixtures and Films. Hybrid nematic precursor mixtures of GO and PBDT solutions were obtained by facile aqueous solution mixing.[19] A representative procedure for obtaining a 1.8 vol % rGO nanocomposite film is given as follows: 1.856 g of a 1 wt % GO dispersion was added to a 20 mL glass vial, followed by dilution with 1.573 g of water. A small stirbar, stirring at 1400 rpm, was used to homogenize the diluted GO (0.541 wt % GO) dispersion. Dropwise, 8.571 g of a 7.0 wt % PBDT solution was added to GO while mixing, resulting in a dark, homogeneous mixture. The resulting PBDT−GO mixture was allowed to mix for 24 h before film-casting. Glass plates were freshly cleaned by soaking in an isopropanol/sodium hydroxide solution, rinsed with deionized water and acetone, and then dried under nitrogen. To cast free-standing PBDT−GO nanocomposite films, ∼3 g of the dispersion was deposited onto a glass plate. An automatic doctor blade set at a 1 mm gap cast the dispersion at a constant linear velocity of 5 mm s^{-1}. The dispersions were placed into a leveled 60 °C oven in air and allowed to dry. The time for complete evaporation was approximately 2 h. Release of the nanocomposite films was accomplished by soaking the film in acetone. The free-standing PBDT−GO nanocomposite films were stored at room temperature for characterization. The concentrations of GO in the final films were calculated using mass density values: ρ_{GO} = 1.8 g mL^{-1} and ρ_{PBDT} = 1.565 g mL^{-1}.[22]

4.5. Tensile and Thermo-Mechanical Characterization. Free-standing nanocomposite films were cut into rectangular strips of an approximate cross-sectional area of 1.5 × 0.03 mm^2 (width × thickness). A 10 mm gauge length was used for both stress−strain and DMTA measurements. All mechanical measurements were performed using an RSA-G2 Solids Analyzer (TA Instruments) equipped with a 32 N load cell. Samples for tensile testing under dry conditions were treated at 200 °C for 20 min to eliminate water. Specimens were tested under dry conditions at 25 °C under a N_2 atmosphere. For all stress−strain measurements, a constant linear displacement rate of 0.1 mm min^{-1} was used. The Young's modulus was calculated by linear regression of the stress−strain curve between 0.15 and 0.3% strain, within the linear viscoelastic regime. Isochronal DMTA measurements used an oscillation frequency of 1 Hz over the temperature range of −150 to 500 °C at a heating rate of 2 °C min^{-1}. Arrhenius analysis of the β-relaxation was accomplished by performing frequency sweeps from 0.1 to 10 Hz over the range of −30 to 110 °C using 5 °C intervals. The sample was allowed to equilibrate for 3 min at each temperature prior to measurements. The temperature of the peak in the loss tangent was determined by differentiation of smooth curves fit to the raw loss tangent data.

4.6. X-ray Scattering. Nanocomposite films were thermally reduced at 200 °C for 20 min under a N_2 atmosphere to match conditions used for mechanical testing. Film strips of approximate dimensions of 60 × 2 × 0.03 mm^3 (length × width × thickness) were cut along the longitudinal direction and folded into eight layers. X-ray scattering (WAXS/SAXS) experiments were performed using a SAXSLab Ganesha equipped with a Cu 50 kV Xenocs Genix ULD SL X-ray source, producing an incident X-ray beam of λ = 1.54 Å and a 2D detector. Sample-to-detector distances of 92, 432, and 1032 mm were used to cover a wide range of scattering vectors. The sample chamber was evacuated and kept at 10^{-2} mbar during measurements to avoid scattering from air. The samples were affixed to a sample holder such that only the nanocomposite film was in the X-ray beam path. For measurements of the polymer alignment in the film plane and along the shear axis, the incident X-ray beam was parallel and orthogonal to the surface normal, respectively. Igor Pro using the Nika package[46] was used for 2D data reduction and analysis.

4.7. Characterization. Optical microscopy was carried out using a Nikon Microphot-FX microscope equipped with polarizing filters. Images were recorded using an OMAX 18 MP digital microscope camera and calibrated with a 0.01 mm calibration slide. All presented micrographs are from samples which have been loaded via capillary action into a 200 μm path length rectangular glass microscopy cell (Vitrotube). Digital photographs were taken with an iPhone 8 Plus in the photo mode. A Hitachi S-4700 cold cathode field emission scanning electron microscope was used for film fracture surface analysis and flake size analysis of GO. Film fracture surfaces were coated with 3 nm of Au prior to analysis. Local mechanical measurements were performed with an Asylum Research Cypher atomic force microscope. Film cross-sectional surfaces for AFM analysis were prepared via cryotome at −55 °C. AFM tests were performed in the amplitude modulation−frequency modulation mode using Si probes with a tip radius of ∼10 nm, a cantilever stiffness of ∼4 N m^{-1}, and a natural frequency of ∼75 kHz. The tips were calibrated on spin-coated polystyrene films; a Hertzian model was used to obtain the elastic modulus. Dispersions of 0.1 wt % were spun-cast onto hydrophilized (O_3 treated for 5 min) Si wafers for flake size analysis. A Kratos Axis Ultra DLD X-ray photoelectron spectrometer operating at 10^{-6} mbar was used for XPS measurements of as-synthesized (dried at 60 °C for 2 h) and thermally reduced (annealed at 200 °C for 2 h) GO films. GO was deposited onto Au@Si substrates prior to analysis. A TGA 5500 (TA Instruments) was utilized for thermogravimetric analysis (TGA) with a 100 μL Pt pan heating at a rate of 10 °C min^{-1} under a N_2 atmosphere.

■ ASSOCIATED CONTENT

Supporting Information

The Supporting Information is available free of charge at https://pubs.acs.org/doi/10.1021/acsami.2c00186.

Dilute solution viscometry in concentrated sulfuric acid and associated discussion, flake size analysis via SEM, TGA of the in situ reduction of LCGO to rGO and resulting nanocomposites, WAXS analysis and azimuthal fitting of scattering intensity, tapping mode AFM of the neat PBDT film, discussion of Arrhenius analysis, and Arrhenius plot for determination of β-relaxation E_a (PDF)

■ AUTHOR INFORMATION

Corresponding Author

Theo J. Dingemans − *Department of Applied Physical Sciences, University of North Carolina at Chapel Hill, Chapel*

https://doi.org/10.1021/acsami.2c00186
ACS Appl. Mater. Interfaces 2022, 14, 16592−16600

Hill, North Carolina 27599-3050, United States; orcid.org/0000-0002-8559-2783; Email: tjd@unc.edu

Authors

Ryan J. Fox − *Department of Applied Physical Sciences, University of North Carolina at Chapel Hill, Chapel Hill, North Carolina 27599-3050, United States;* orcid.org/0000-0002-1472-6262

Maruti Hegde − *Department of Applied Physical Sciences, University of North Carolina at Chapel Hill, Chapel Hill, North Carolina 27599-3050, United States*

Daniel P. Cole − *DEVCOM Army Research Laboratory, Aberdeen Proving Ground, Maryland 21005, United States*

Robert B. Moore − *Department of Chemistry, Macromolecules Innovation Institute, Blacksburg, Virginia 24061, United States;* orcid.org/0000-0001-9057-7695

Stephen J. Picken − *Faculty of Applied Sciences, Delft University of Technology, Delft 2629 HZ, The Netherlands;* orcid.org/0000-0002-6003-518X

Complete contact information is available at: https://pubs.acs.org/10.1021/acsami.2c00186

Notes

The authors declare no competing financial interest.

■ ACKNOWLEDGMENTS

The authors would like to thank A. Kumbhar for assisting with SEM measurements, C. Donley for performing the XPS experiments, and J. Gair for help with cryotome surface preparation. This material is based upon work supported by, or in part by, the U.S. Army Research Laboratory and the U.S. Army Research Office under contract number A17-0053-001. This work was performed in part at the Chapel Hill Analytical and Nanofabrication Laboratory (CHANL) and the Duke Shared Materials Instrumentation Facility (SMIF) and by members of the North Carolina Research Triangle Nanotechnology Network (RTNN), which is supported by the National Science Foundation, Grant ECCS-1542015, as part of the National Nanotechnology Coordinated Infrastructure (NNCI).

■ REFERENCES

(1) Chen, J.; Ramasubramaniam, R.; Xue, C.; Liu, H. A Versatile, Molecular Engineering Approach to Simultaneously Enhanced, Multifunctional Carbon-Nanotube- Polymer Composites. *Adv. Funct. Mater.* **2006**, *16*, 114−119.

(2) Naskar, A. K.; Keum, J. K.; Boeman, R. G. Polymer Matrix Nanocomposites for Automotive Structural Components. *Nat. Nanotechnol.* **2016**, *11*, 1026−1030.

(3) Hu, K.; Kulkarni, D. D.; Choi, I.; Tsukruk, V. V. Graphene-Polymer Nanocomposites for Structural and Functional Applications. *Prog. Polym. Sci.* **2014**, *39*, 1934−1972.

(4) Njuguna, J.; Pielichowski, K. Polymer Nanocomposites for Aerospace Applications: Properties. *Adv. Eng. Mater.* **2003**, *5*, 769−778.

(5) Young, R. J.; Kinloch, I. A.; Gong, L.; Novoselov, K. S. The Mechanics of Graphene Nanocomposites: A Review. *Compos. Sci. Technol.* **2012**, *72*, 1459−1476.

(6) Papageorgiou, D. G.; Kinloch, I. A.; Young, R. J. Mechanical Properties of Graphene and Graphene-Based Nanocomposites. *Prog. Mater. Sci.* **2017**, *90*, 75−127.

(7) Kinloch, I. A.; Suhr, J.; Lou, J.; Young, R. J.; Ajayan, P. M. Composites with Carbon Nanotubes and Graphene: An Outlook. *Science* **2018**, *362*, 547−553.

(8) Gong, L.; Young, R. J.; Kinloch, I. A.; Riaz, I.; Jalil, R.; Novoselov, K. S. Optimizing the Reinforcement of Polymer-Based Nanocomposites by Graphene. *ACS Nano* **2012**, *6*, 2086−2095.

(9) Pang, Y.; Yang, J.; Curtis, T. E.; Luo, S.; Huang, D.; Feng, Z.; Morales-Ferreiro, J. O.; Sapkota, P.; Lei, F.; Zhang, J.; Zhang, Q.; Lee, E.; Huang, Y.; Guo, R.; Ptasinska, S.; Roeder, R. K.; Luo, T. Exfoliated Graphene Leads to Exceptional Mechanical Properties of Polymer Composite Films. *ACS Nano* **2019**, *13*, 1097−1106.

(10) Xu, Z.; Gao, C. Aqueous Liquid Crystals of Graphene Oxide. *ACS Nano* **2011**, *5*, 2908−2915.

(11) Xu, Z.; Gao, C. Graphene Chiral Liquid Crystals and Macroscopic Assembled Fibres. *Nat. Commun.* **2011**, *2*, 571.

(12) Kim, J. E.; Han, T. H.; Lee, S. H.; Kim, J. Y.; Ahn, C. W.; Yun, J. M.; Kim, S. O. Graphene Oxide Liquid Crystals. *Angew. Chem. Int. Ed.* **2011**, *50*, 3043−3047.

(13) Dan, B.; Behabtu, N.; Martinez, A.; Evans, J. S.; Kosynkin, D. V.; Tour, J. M.; Pasquali, M.; Smalyukh, I. I. Liquid Crystals of Aqueous, Giant Graphene Oxide Flakes. *Soft Matter* **2011**, *7*, 11154−11159.

(14) Aboutalebi, S. H.; Gudarzi, M. M.; Zheng, Q. B.; Kim, J.-K. Spontaneous Formation of Liquid Crystals in Ultralarge Graphene Oxide Dispersions. *Adv. Funct. Mater.* **2011**, *21*, 2978−2988.

(15) Hu, X.; Xu, Z.; Liu, Z.; Gao, C. Liquid Crystal Self-Templating Approach to Ultrastrong and Tough Biomimic Composites. *Sci. Rep.* **2013**, *3*, 2374.

(16) Liu, Z.; Xu, Z.; Hu, X.; Gao, C. Lyotropic Liquid Crystal of Polyacrylonitrile-Grafted Graphene Oxide and Its Assembled Continuous Strong Nacre-Mimetic Fibers. *Macromolecules* **2013**, *46*, 6931−6941.

(17) Yousefi, N.; Gudarzi, M. M.; Zheng, Q.; Aboutalebi, S. H.; Sharif, F.; Kim, J.-K. Self-alignment and high electrical conductivity of ultralarge graphene oxide-polyurethane nanocomposites. *J. Mater. Chem.* **2012**, *22*, 12709−12717.

(18) Jalili, R.; Aboutalebi, S. H.; Esrafilzadeh, D.; Shepherd, R. L.; Chen, J.; Aminorroaya-Yamini, S.; Konstantinov, K.; Minett, A. I.; Razal, J. M.; Wallace, G. G. Scalable One-Step Wet-Spinning of Graphene Fibers and Yarns from Liquid Crystalline Dispersions of Graphene Oxide: Towards Multifunctional Textiles. *Adv. Funct. Mater.* **2013**, *23*, 5345−5354.

(19) Hegde, M.; Yang, L.; Vita, F.; Fox, R. J.; van de Watering, R.; Norder, B.; Lafont, U.; Francescangeli, O.; Madsen, L. A.; Picken, S. J.; Samulski, E. T.; Dingemans, T. J. Strong Graphene Oxide Nanocomposites from Aqueous Hybrid Liquid Crystals. *Nat. Commun.* **2020**, *11*, 830.

(20) Wang, Y.; He, Y.; Yu, Z.; Gao, J.; Ten Brinck, S.; Slebodnick, C.; Fahs, G. B.; Zanelotti, C. J.; Hegde, M.; Moore, R. B.; Ensing, B.; Dingemans, T. J.; Qiao, R.; Madsen, L. A. Double Helical Conformation and Extreme Rigidity in a Rodlike Polyelectrolyte. *Nat. Commun.* **2019**, *10*, 801.

(21) Wang, Y.; Chen, Y.; Gao, J.; Yoon, H. G.; Jin, L.; Forsyth, M.; Dingemans, T. J.; Madsen, L. A. Highly Conductive and Thermally Stable Ion Gels with Tunable Anisotropy and Modulus. *Adv. Mater.* **2016**, *28*, 2571−2578.

(22) Gao, J.; Wang, Y.; Norder, B.; Garcia, S. J.; Picken, S. J.; Madsen, L. A.; Dingemans, T. J. Water and Sodium Transport and Liquid Crystalline Alignment in a Sulfonated Aramid Membrane. *J. Membr. Sci.* **2015**, *489*, 194−203.

(23) Wang, Y.; Gao, J.; Dingemans, T. J.; Madsen, L. A. Molecular Alignment and Ion Transport in Rigid Rod Polyelectrolyte Solutions. *Macromolecules* **2014**, *47*, 2984−2992.

(24) Wu, Z. L.; Arifuzzaman, M.; Kurokawa, T.; Le, K.; Hu, J.; Sun, T. L.; Furukawa, H.; Masunaga, H.; Gong, J. P. Supramolecular Assemblies of a Semirigid Polyanion in Aqueous Solutions. *Macromolecules* **2013**, *46*, 3581−3586.

(25) Yang, W.; Furukawa, H.; Shigekura, Y.; Shikinaka, K.; Osada, Y.; Gong, J. P. Self-Assembling Structure in Solution of a Semirigid Polyelectrolyte. *Macromolecules* **2008**, *41*, 1791−1799.

(26) Funaki, T.; Kaneko, T.; Yamaoka, K.; Ohsedo, Y.; Gong, J. P.; Osada, Y.; Shibasaki, Y.; Ueda, M. Shear-Induced Mesophase

Organization of Polyanionic Rigid Rods in Aqueous Solution. *Langmuir* **2004**, *20*, 6518−6520.
(27) Sarkar, N.; Kershner, L. D. Rigid Rod Water-Soluble Polymers. *J. Appl. Polym. Sci.* **1996**, *62*, 393−408.
(28) Fox, R. J.; Chen, W.-R.; Do, C.; Picken, S. J.; Forest, M. G.; Dingemans, T. J. Fingerprinting the Nonlinear Rheology of a Liquid Crystalline Polyelectrolyte. *Rheol. Acta* **2020**, *59*, 727−743.
(29) Fox, R. J.; Hegde, M.; Zanelotti, C. J.; Kumbhar, A. S.; Samulski, E. T.; Madsen, L. A.; Picken, S. J.; Dingemans, T. J. Irreversible Shear-Activated Gelation of a Liquid Crystalline Polyelectrolyte. *ACS Macro. Lett.* **2020**, *9*, 957−963.
(30) Fox, R. J.; Forest, M. G.; Picken, S. J.; Dingemans, T. J. Observation of Transition Cascades in Sheared Liquid Crystalline Polymers. *Soft Matter* **2020**, *16*, 3891−3901.
(31) Mundoor, H.; Park, S.; Senyuk, B.; Wensink, H. H.; Smalyukh, I. I. Hybrid Molecular-Colloidal Liquid Crystals. *Science* **2018**, *360*, 768−771.
(32) Hummers, W. S.; Offeman, R. E. Preparation of Graphitic Oxide. *J. Am. Chem. Soc.* **1958**, *80*, 1339.
(33) Fox, R. J.; Yu, D.; Hegde, M.; Kumbhar, A. S.; Madsen, L. A.; Dingemans, T. J. Nanofibrillar Ionic Polymer Composites Enable High-Modulus Ion-Conducting Membranes. *ACS Appl. Mater. Interfaces* **2019**, *11*, 40551−40563.
(34) Mattevi, C.; Eda, G.; Agnoli, S.; Miller, S.; Mkhoyan, K.A.; Celik, O.; Mastrogiovanni, D.; Granozzi, G.; Garfunkel, E.; Chhowalla, M. Evolution of Electrical, Chemical, and Structural Properties of Transparent and Conducting Chemically Derived Graphene Thin Films. *Adv. Funct. Mater.* **2009**, *19*, 2577−2583.
(35) Every, H. A.; Mendes, E.; Picken, S. J. Ordered Structures in Proton Conducting Membranes from Supramolecular Liquid Crystal Polymers. *J. Phys. Chem. B* **2006**, *110*, 23729−23735.
(36) Picken, S. J.; Aerts, J.; Visser, R.; Northolt, M. G. Structure and rheology of aramid solutions: x-ray scattering measurements. *Macromolecules* **1990**, *23*, 3849−3854.
(37) Zlopasa, J.; Norder, B.; Koenders, E. A. B.; Picken, S. J. Origin of Highly Ordered Sodium Alginate/Montmorillonite Bionanocomposites. *Macromolecules* **2015**, *48*, 1204−1209.
(38) Vallés, C.; Young, R. J.; Lomax, D. J.; Kinloch, I. A. The Rheological Behaviour of Concentrated Dispersions of Graphene Oxide. *J. Mater. Sci.* **2014**, *49*, 6311−6320.
(39) Fan, S. M.; Luckhurst, G. R.; Picken, S. J. A Deuterium Nuclear Magnetic Resonance Investigation of Orientational Order and Director Kinetics in Aramid Solutions. *J. Chem. Phys.* **1994**, *101*, 3255−3267.
(40) Picken, S. J.; van der Zwaag, S.; Northolt, M. G. Molecular and Macroscopic Orientational Order in Aramid Solutions: a Model to Explain the Influence of Some Spinning Parameters on the Modulus of Aramid Yarns. *Polymer* **1992**, *33*, 2998−3006.
(41) Frosini, V.; Butta, E. Some remarks on the mechanical relaxations in aliphatic, partially aromatic and wholly aromatic polyamides. *Polym. Lett.* **1971**, *9*, 253−260.
(42) Kunugi, T.; Watanabe, H.; Hashimoto, M. Dynamic Mechanical Properties of Poly(p-phenylene terephthalamide) Fiber. *J. Appl. Polym. Sci.* **1979**, *24*, 1039−1051.
(43) Yemni, T.; Boyd, R. H. A Dielectric Study of the Amorphous Fraction in Oriented Nylon 610. *J. Polym. Sci., Polym. Phys. Ed.* **1976**, *14*, 499−508.
(44) Serpe, G.; Chaupart, N. Relaxation-Structure Relationship in Bulk and Plasticized Polyamide 11. *J. Polym. Sci., Part B: Polym. Phys.* **1996**, *34*, 2351−2365.
(45) Zero, K.; Aharoni, S. M. Depolarization Ratios and Rigidity of Aromatic Polyamides. *Macromolecules* **1987**, *20*, 1957−1960.
(46) Ilavsky, J. Nika: Software for Two-Dimensional Data Reduction. *J. Appl. Crystallogr.* **2012**, *45*, 324−328.

https://doi.org/10.1021/acsami.2c00186
ACS Appl. Mater. Interfaces 2022, 14, 16592−16600